Assessment of general and localized corrosion behavior of X65 and 13Cr steels in water-saturated supercritical CO_2 environments with SO_2/O_2

Yong Hua*[a], Raghu Jonnalagadda[a], Lei Zhang[b], Anne Neville[a] and Richard Barker[a]

[a] Institute of Functional Surfaces, School of Mechanical Engineering, University of Leeds, Leeds, LS2 9JT, UK

[b] Corrosion and Protection Centre, University of Science and Technology Beijing, 30 Xueyuan Road, Beijing, China

*Corresponding author: Yong Hua, Tel: 07923359918, Email: leo.huayong@gmail.com

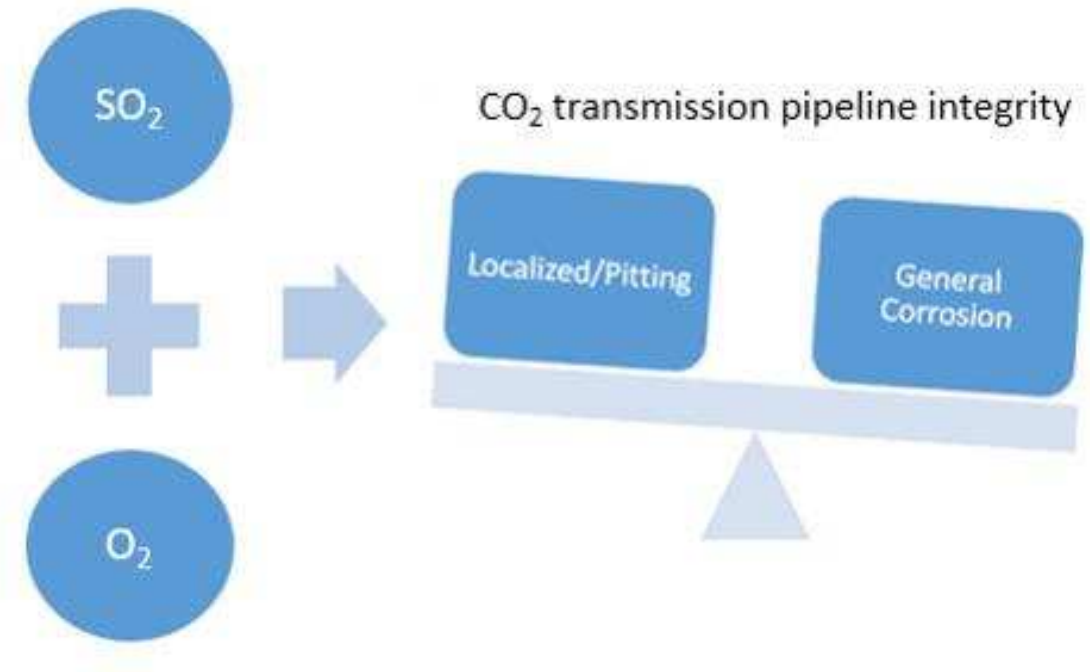

Abstract

To mitigate the corrosive effect encountered in carbon steel pipelines during dense phase CO_2 transport the general consensus is that the CO_2 stream must be sufficiently dehydrated. Although such a process will undoubtedly help prevent the breakout of free water, it can contribute significantly towards the handling costs, particularly in the context of offshore installations. As opposed to drying the CO_2 stream to excessive levels, one alternative option

is the application of corrosion resistant alloys such as 13Cr. This paper performs a comparison between X65 carbon steel and 13Cr in pure and impure CO_2, evaluating the influence of SO_2 and O_2 on the general and localized corrosion rate of both materials at 80 bar and 35 °C. The results show that 13Cr is able to perform exceptionally well in comparison to X65 in pure CO_2 as well as when SO_2 and O_2 are present in the system individually, producing no localized corrosion and general corrosion rates below 0.02 mm/y. However, when SO_2 and O_2 were combined, the formation of sulfuric acid was permitted which proved detrimental to 13Cr, producing excessive localized attack much greater than that observed on X65. Raman spectrosopy, XRD and SEM/EDX are used to analyse the corrosion products

Key words: CO_2 corrosion, carbon steel, carbon capture and storage, sulfur dioxide, oxygen

1. Introduction

Fossil fuels will continue to be the dominant source of the world's energy production for the foreseeable future, yet there has been increased concern that the combustion of such carbon-based fuels produces greenhouse gases (particularly CO_2), which adversely affect the global climate.[1]

The implementation of Carbon Capture and Storage (CCS) technology would allow the continued use of fossil fuels through the abatement of carbon dioxide (CO_2), preventing emissions into the atmosphere. Currently, CCS is the only process available to generate a significant and immediate impact on the Earth's environment.

CCS refers to a process by which CO_2 is captured from large point sources (e.g. power generation and industrial applications), followed by compression and transportation to a storage site (e.g. a geological reservoir or depleted oil field). For the transmission of large

quantities of CO_2, the most logical and cost effective solution would be the development of a dedicated pipeline network manufactured from carbon steel to transport CO_2 in a liquid or supercritical state. However, one limitation of carbon steel is its susceptibility to corrosion in flue gas environments due to the presence of CO_2, water (H_2O), oxygen (O_2), sulfur dioxide (SO_2), nitrogen oxides (NO_x) and other constituents that can result in the formation of corrosive phases.

A number of studies have recently been published which seek to understand the implications of such impurities in liquid or supercritical CO_2 on the extent of carbon steel corrosion during pipeline transportation.[2-20] Research has also focused on defining the safe limits of impurities that can be tolerated within the CO_2 stream by systematically varying the water content or concentration of other contaminants such as SO_2, O_2 and NO_x amongst others.[4, 5, 7, 9, 18, 20, 33, 34, 35, 36]

From a review of the literature within this subject area it appears that in order to appropriately mitigate excessive corrosion rates the general consensus is that sufficient drying (i.e. water removal) of impure CO_2 upstream of the pipeline is required. Although such a process can prevent the breakout of free water, it can contribute significantly towards handling costs, particularly in the context of offshore installations.[1] Furthermore, some studies have suggested that extensive dehydration down to 50 ppm (mole) should be applied, which can require the use of molecular sieves, imposing an even greater cost[9, 32]. Limits as low as 50 ppm have already been implemented in the US[21] and Norway[22] for specific pipelines. However, other specifications from the DYNAMIS project[23] and for the Kinder Morgan pipeline[24] are less conservative, imposing limits of 500 and 650 ppm, respectively.

As opposed to dehydrating the CO_2 stream, one alternative option is the application of corrosion resistant alloys (CRAs) such as 13Cr. However, limited data on CRA corrosion in dense phase CO_2 is available in the literature with the exception of work by Choi et al.[16] which was performed with 13Cr in the presence of very high SO_2/O_2 concentrations (1% and 5%, respectively) that are orders of magnitude greater than those typically anticipated for anthropogenic CO_2 transport according to Walspurger et al.[25].

The purpose of this present study is to contribute to the literature by determining the ability of 13Cr relative to X65 carbon steel to mitigate corrosion in water-saturated dense phase CO_2 when SO_2 and O_2 are present both individually and together. Both the general and localized corrosion behavior of X65 and 13Cr are determined using white light interferometry and the nature and morphology of corrosion products formed on the steel surface are reviewed using a combination of scanning electron microscopy (SEM), energy dispersive X-ray spectroscopy (EDX), and X-ray diffraction (XRD) in order to clarify the role low concentrations of SO_2 and O_2 play in the degradation process and ascertain whether selection of a CRA is a suitable corrosion mitigation option.

2. Experimental procedure

2.1 Sample preparation

Test specimens were machined into discs of diameter 25 mm and thickness of 6 mm from both API 5L X65 carbon steel and 13Cr (UNS41000) bars. The chemical composition of X65 and 13Cr and their microstructures are provided in Table 1 and Figure 1 respectively. Surface preparation for corrosion experiments consisted of wet-grinding the entire sample with up to 600 grit silicon carbide abrasive paper, rinsing with distilled water, followed by acetone and high purity ethanol, followed by drying gently with compressed air. Samples were then stored

in a desiccator until required and weighed immediately before the experiment on an electronic balance to within an accuracy of 0.01 mg before suspending inside the autoclave. Two samples of the same material were placed within the autoclave for each individual test. Surface preparation for the microstructures consisted of wet-grinding the entire sample surface up to 1200 grit silicon carbide abrasive paper, followed by polishing with the help of 3µm diamond suspension to attain a mirror finish, rinsing with distilled water, followed by acetone, high purity ethanol and drying gently with compressed air. Etchants were varied depending on the sample alloy composition. A 2% Nital was used for X65 where etching consisted of swabbing the surface for 10-20 seconds with a cotton pad. 13Cr was etched with waterless Kalling's reagent (5 g copper chloride + 100 ml hydrochloric acid + 100 ml ethanol) by swabbing the surface for 10 seconds with a cotton pad.

2.2 Autoclave testing procedure

A schematic representation of the autoclave experimental system layout is provided in Figure 2. The testing procedure has been published in a previous paper. [7]

All tests were conducted under static conditions in water-saturated supercritical CO_2 (a water content of 3437 ppm in the dense phase at 80 bar and 35°C based on the analysis performed by Spycher et al.[26]). However, in order to ensure complete saturation of CO_2 under these conditions, 34000 ppm of water was introduced to the bottom of the autoclave (i.e. not in direct contact with the sample). The entire matrix of the experimental conditions is provided in Table 2 which describes the different materials and conditions that were evaluated. The molar concentrations of SO_2 (100 ppm) and O_2 (1000 ppm) were specifically chosen to reflect the recommended limits proposed by de Visser et al.[23] and Alstom (which can be found in a

110 publication by Dugstad et al.[13]) to ensure safe CO_2 transport. However, it should be noted
111 that the proposed limits within these publications are based on health and safety criteria in
112 the event of a sudden release from a pipeline, not from the perspective of corrosion/pipeline
113 integrity. This study aims to evaluate whether these proposed limits are tolerable within a
114 CO_2 pipeline when the stream is saturated with water. Previous research [37, 38] has indicated
115 that the addition of these particular impurities at the aforementioned concentrations do not
116 shift the critical point of CO_2 significantly. As such, all experiments performed in this study are
117 conducted with CO_2 within its supercritical state.

118 It is difficult to monitor the actual pH of the solution due to the presence of small amounts of
119 water in the system and the considerable pressure. Consequently, the OLI software [31] was
120 used to speculate about the possible pH of the aqueous phase as shown in Figure 3.
121 Considering the experimental conditions in this work (35°C and 80 bar CO_2), the solution pH
122 is expected to reduce from 3.1 in the absence of SO_2 to 2.4 when 100 ppm SO_2 is introduced.
123 This is based on the assumption that SO_2 will partially dissolve into the aqueous phase to form
124 sulfurous acid (H_2SO_3) as stated by Dugstad et al.[10] It is difficult to predict the effect of
125 combined addition of O_2 and SO_2 to this system. However, based on the assumption that the
126 likely effect is to promote the formation of sulfuric acid through the oxidation of sulfurous
127 acid, the pH can be expected to decrease markedly given that sulfuric acid is a much stronger
128 acid.

129 At the end of each experiment, the specimens were dried thoroughly and subsequently
130 chemically cleaned to remove all traces of corrosion products before weighing. The cleaning
131 process consisted of wiping the surface with a cotton pad soaked in Clarke's solution (20 g
132 antimony trioxide + 50 g stannous chloride + 1000 ml hydrochloric acid) in accordance with

ASTM Standard G1-03[27]. This was followed by rinsing the samples with distilled water and then drying with compressed air.

The mass loss due to corrosion was determined from the weight difference before exposure and after cleaning. The corrosion rates were calculated using Equation (1):

$$V_c = \frac{87600\Delta m}{\rho A t} \quad (1)$$

where V_c is the corrosion rate of the sample in mm/year, Δm is the weight loss in grams, ρ is the density of the sample in g/cm^3, A is the exposed area in cm^2 and t is the immersion time in hours.

3. Results and Discussion

3.1 General corrosion of X65 and 13Cr steels exposed to water-saturated supercritical CO_2 condition with various SO_2/O_2 concentrations

Figure 4 provides the general corrosion rates recorded (based on gravimetric analysis) for X65 and 13Cr exposed to water-saturated conditions in the presence of various concentrations of SO_2 and O_2. In the absence of SO_2 and O_2, the general corrosion rates of X65 and 13Cr are 0.1 and 0.003 mm/y, respectively. Addition of 1000 ppm O_2 serves to reduce the general corrosion rates of both materials to 0.03 and 0.001 mm/year. The ability of O_2 to reduce the general corrosion of carbon steel in CO_2 systems has been reported previously by other authors at low temperatures and can be attributed to the formation of protective oxide films on the steel surface[5, 28]. In terms of 13Cr, O_2 is also known to assist in the formation and replenishment of the passive chromium oxide films that can be established on the steel surface, which can explain the increase in general corrosion resistance with the introduction of O_2.

154 The mass loss measurements in Figure 4 indicate that O_2 has no detrimental effect on the
155 general corrosion of X65 and 13Cr in a CO_2-H_2O-O_2 system under these particular conditions
156 and that 13Cr exhibits improved corrosion resistance compared to X65 in both environments.
157 The superiority of 13Cr relative to X65 in CO_2-H_2O and CO_2-H_2O-O_2 systems at high pressure
158 was also reported by Choi et al.[16] for experiments performed at 80 bar and 50°C in CO_2-
159 satuarted water. However, in contrast to the results in Figure 4, Choi et al.[16] reported an
160 increase in general corrosion rates of X65 for experiments in water-saturated CO_2 with the
161 introduction of O_2. A possible explanation for the disparity in observations could be linked to
162 the temperature difference in experiments, but also the higher O_2 contents of 1.6-5.5 bar
163 evaluated by Choi et al., [16]. As O_2 content and temperature are increased, O_2 is capable of
164 influencing the kinetics of the cathodic reaction at the steel surface (see Equation (2) for the
165 reaction under acidic environments), which may explain the accelerated corrosion reported
166 by Choi and co-workers. [16]

$$O_2 + 4H^+ + 4e^- \rightarrow 2H_2O \quad (2)$$

167

168 Referring again to Figure 4, the introduction of solely 100 ppm SO_2 to the CO_2 system resulted
169 in an increase in general corrosion rates of X65 and 13Cr from 0.1 and 0.003 mm/y to 0.65
170 and 0.01 mm/y, respectively. Generally, the acceptable internal corrosion limit for such
171 pipelines is ~0.1 mm/y, although this depends on the system design life and the anticipated
172 corrosivity of the fluid being transported. For the sake of material evaluation, adopting 0.1
173 mm/y as an acceptable benchmark, the corrosion rate of X65 under these conditions is well
174 beyond this limit, whereas 13Cr is still able to offer adequate corrosion protection even in a
175 water-saturated environment.

Addition of both 100 ppm SO_2 and 1000 ppm O_2 (final column in Figure 4) clearly enhances the corrosion rate of both materials from the pure CO_2 environment, particularly in the case of 13Cr. The general corrosion rates recorded were 0.95 and 0.75 mm/y for X65 and 13Cr, respectively. The collection of results within Figure 4 indicate a noticeable synergistic effect between SO_2 and O_2. Corrosion rates observed when SO_2 and O_2 are together exceed the sum of the two individual degradation rates when the both species are present individually. The observed synergistic effect is evident in both materials and results in 13Cr exceeding 0.1 mm/y by a large margin (by 0.65 mm/year), making it an unsuitable material choice for such an environment based on this reported limit.

3.2 Corrosion product morphology for X65

Figure 5 shows the SEM images of the X65 steel surface after 48 h exposure to the water-saturated CO_2 phase containing different concentrations of SO_2 and O_2. In the absence of SO_2 and O_2, iron carbonate ($FeCO_3$) is the sole crystalline product recorded on the steel surface (Figure 5(a)) and this is confirmed by the XRD pattern provided in Figure 6. Addition of 1000 ppm O_2 inhibited the formation of $FeCO_3$, producing a seemingly amorphous corrosion product layer which produced no XRD pattern within Figure 6. XPS analysis of the film in a previous publication identified that the film formed under these conditions predominantly comprises of iron oxides and/or hydroxides[5]. It is assumed that the oxidation of Fe^{2+} to Fe^{3+} due to the presence of O_2 inhibits the formation of $FeCO_3$.

Addition of solely 100 ppm SO_2 (SEM image in Figure 5(c)) produced a corrosion product layer comprising of both $FeCO_3$ and iron sulfite ($FeSO_3$) according to the XRD pattern provided in Figure 6. This was confirmed by additional Raman spectroscopy measurements performed on the same sample. The introduction of both 100 ppm SO_2 and 1000 ppm O_2 resulted in the

199 formation of $FeCO_3$ and $FeSO_3$ (confirmed by XRD patterns in Figure 6), but also the co-
200 presence of hydrated $FeSO_4$ based on localized Raman spectra (specifically peaks at 185, 480
201 and 990 cm^{-1}[29] identified within Figure 7).

202 These observations are in alignment with Choi et al.[16] who reported that the presence of SO_2
203 alone promoted the formation of $FeSO_3$ on X65 steel while the addition of O_2 can form $FeSO_4$.
204 The work is also in alignment with Dugstad et al.[10] who stated that the presence of SO_2
205 permits the formation of sulfurous acid (H_2SO_3), and the addition of O_2 enables sulfuric acid
206 (H_2SO_4) to be formed via the series of reactions (3) to (5). H_2SO_4 is a significantly stronger acid
207 then H_2SO_3, and is potentially more corrosive, corroborating with the observed synergistic
208 effect between O_2 and SO_2.

$$H_2O + SO_2 \rightarrow H^+ + HSO_3^- \quad (3)$$

$$HSO_3^- \rightarrow H^+ + SO_3^{2-} \quad (4)$$

$$SO_3^{2-} + \frac{1}{2}O_2 \rightarrow SO_4^{2-} \quad (5)$$

209 The formation of sulfite and sulfate ions enables the precipitation of $FeSO_3$ and $FeSO_4$ via
210 precipitation reactions:

$$Fe^{2+} + SO_3^{2-} \rightarrow FeSO_3 \quad (6)$$

$$Fe^{2+} + SO_4^{2-} \rightarrow FeSO_4 \quad (7)$$

211 while $FeCO_3$ is produced from the precipitation of iron and bicarbonate ions formed from the
212 steel dissolution and dissociation of carbonic acid within the aqueous phase:

$$Fe^{2+} + CO_3^{2-} \rightarrow FeCO_3 \quad (8)$$

3.3 Corrosion product morphology for 13Cr

13Cr samples exposed to 0 ppm SO_2 with and without 1000 ppm O_2 produced general corrosion rates below 0.003 mm/year, indicating that O_2 presence has little effect on the general corrosion of the CRA. SEM images of the steel surface indicated no noticeable signs of general or localized corrosion and are provided in Figure 8. SEM images of the 13Cr surface after exposure to 100 ppm SO_2 with and without 1000 ppm O_2 are provided in Figure 9 and show clear signs of material degradation as a result of introducing SO_2, the presence of SO_2 permits the formation of H_2SO_3 and the addition of O_2 enables H_2SO_4 to be formed. Both H_2SO_3 and H_2SO_4 are more corrosive in comparison to that of H_2CO_3, corroborating with the increased mass loss observed. No significant corrosion product was visible on the 13Cr surface exposed to solely 100 ppm SO_2 (Figure 9(a)) as degradation rates under these conditions were still low at 0.01 mm/y and unlikely to result in substantial corrosion product precipitation. However, the combined presence of SO_2 and O_2 resulted in corrosion rates rising to 0.65 mm/y, producing a thin, cracked corrosion product layer (Figure 9(b)).

XRD and Raman analysis of the corrosion product observed in the SEM image shown in Figure 9(b) proved challenging and were unable to identify the nature of the corrosion product present. However, cross-section EDX analysis of the films formed on X65 and 13Cr after exposure to 100 ppm SO_2 and 1000 ppm O_2 after 6 h and 48 h (Figure 10) showed that the thickness of the corrosion products increased for both materials and the corrosion product on 13Cr was rich in Cr, S and O, and contained very little traces of Fe. Given that the combined presence of O_2 and SO_2 permits the formation of H_2SO_4, as discussed by Dugstad et al.[10], it is suggested that this acid is capable of dissolving the Cr_2O_3 passive film and reacting with Cr^{3+}

235 to produce chromium sulfate ($Cr_2(SO_4)_3$), although this cannot be confirmed and requires
236 further study.
237
238 **3.4 Localized corrosion of X65 and 13Cr**
239 One particular concern in acidic environments, particularly in CRAs is the potential for
240 localized corrosion to occur. Each material and test environment combination considered in
241 Figure 1 (and Table 2) was evaluated for localized attack using white-light interferometry. The
242 threshold value used was 1 μm and so the measured localized depth beneath that value of
243 depth will not be considered. An example of profilometry images of X65 and 13Cr sample
244 surface exposure to water-saturated CO_2 condition in the presence of 100 ppm SO_2 and 1000
245 ppm O_2 are provided in Figure 11. Smaller versions of these images are also embedded within
246 Figure 12 which provides a summary of the pit/localized depth measurements extracted from
247 X65 and 13Cr samples from all tests performed in Figure 1 and are expressed as penetration
248 rates. The localized/pit depth analysis was conducted in alignment with ASTM Standard G46-
249 94, selecting the average of the 10 deepest pits on the surface to provide an accurate
250 assessment[30]. Multiple scans (at least 3) such as those shown in Figure 11 were performed
251 across the steel surface to ensure reliable data was obtained.

252 Considering Figure 12, it is evident that X65 steel undergoes localized attack in all
253 environments. The attack manifests itself as a form of micro-pitting over 48 h (typical image
254 shown in Figure 11) and is particularly prominent in the presence of 1000 ppm O_2 and 100
255 ppm SO_2/1000 ppm O_2, exceeding pitting rates of 2 mm/year. In contrast, 13Cr was only
256 susceptible to localized corrosion when both SO_2 and O_2 were present together. Under these
257 conditions, the form of corrosion observed was a combination of extensive localized attack

and pitting, with the surrounding material adjacent to the attack undergoing significantly less attack. SEM images of the X65 and 13Cr surfaces after 6h and 48 h of exposure are provided in Figure 13. These images were taken after cleaning with Clarke's solution and etching the steel surface; they indicate that the pit initiation is not limited to solely the ferrite phase of the material for X65 steel.

3.5 100 ppm SO_2 and 1000 ppm O_2 – evolution of corrosion products and general/localized corrosion rate vs time

The initial localized depth measurements at 48 h in the previous section cast ambiguity over the actual growth of pits/localized areas as they are purely one measurement performed at a particular instance in time. To determine the nature of surface pit growth/rate of localized attack, X65 and 13Cr samples were exposed to the 100 ppm SO_2/1000 ppm O_2 environment for varying exposure times between 6 and 48 h. After each experiment, gravimetric measurements and surface profilometry were performed on both materials to determine the general and localized corrosion rates, respectively. The data collected is provided in Figure 14 and shows that there is little difference between the general corrosion rate of X65 and 13Cr over 48 h of exposure. However, a difference of one order of magnitude is recorded between X65 and 13Cr in terms of localized attack, with 13Cr showing much greater susceptibility to the SO_2/O_2 environment than X65 steel. Both materials display decay in their rate of localized attack as a function of time. The actual general and localized corrosion rates could be higher than the values recorded here due to depletion of impurities in a closed autoclave over time. However, the localized attack for both materials remain high for the duration of the experiment.

The evolution of corrosion products on the surface of X65 and 13Cr is provided in Figure 15 and indicates the presence of a sulfur-rich, cracked film as early as 6 h into the experiment on both materials. Further work is still needed to determine when exactly pit nucleation starts to occur and what causes this process. Additionally, further work is required to determine whether the reduction in localized corrosion rate is attributed to corrosion product formation in the localized region, re-passivation of the oxide film or depletion of impurities within the autoclave.

Conclusions

The research presented has focused towards studying and quantifying the extent of both general and localized corrosion of X65 and 13Cr in water-saturated supercritical CO_2 environments containing various SO_2 and O_2, representative of dense phase CO_2 transport. Tests were conducted at a pressure of 80 bar and a temperature of 35°C for periods of up to 48 h. The main conclusions which can be drawn from this study are:

- The general and localized corrosion rate of X65 in water-saturated dense-phase environments is accentuated by the presence of 100 ppm SO_2 and 100 ppm SO_2/1000 ppm O_2. The effect of 1000 ppm O_2 as a sole impurity served to reduce general corrosion rates, but promotes more substantial pitting on the steel surface.
- The most aggressive environment for X65 was obtained when SO_2 and O_2 were combined together which produced general corrosion rates of 0.95 mm/y. SO_2 alone in the water-saturated dense phase CO_2 permits the formation of sulfurous acid, which resulted in the precipitation of $FeSO_3$ on the steel surface. However, the addition of O_2 was shown to result in the formation of SO_4^{2-} (through the formation of sulphuric acid), producing $FeSO_4$ on the steel surface.
- 13Cr was shown to be highly resistant to corrosion in the CO_2-H_2O-O_2 and CO_2-H_2O environments, producing no indication of localized attack and general corrosion rates below 0.003 mm/y. The material also performed well in experiments with 100 ppm SO_2 present, producing no signs of localized corrosion and general corrosion rates below 0.02 mm/y.

- The combined presence of O_2 and SO_2 was detrimental to 13Cr, producing general corrosion rates of 0.65 mm/y. A clear synergistic effect was observed between SO_2 and O_2 for both X65 and 13Cr whereby the degradation rates resulting from the combined presence exceeded the total of the corrosion rates produced when the species were present individually.
- Pitting rates of X65 and 13Cr were shown to be in excess of 7 and 80 mm/year at the start of the experiment for X65 and 13Cr, respectively. The pitting rates were shown to reduce with time by around an order of magnitude. If was not clear whether the reduction in corrosion rate was attributed to corrosion product formation, pit repassivation or depletion of impurities within the system.

References

1. G.A. Jacobson, S. Kerman, Y.-S. Choi, A. Dugstad, S. Nesic, and S. Papavinasam, "Pipeline Corrosion Issues Related to Carbon Capture, Transportation, and Storage", Materials Performance, (2014): p. 24-31.
2. Y. Hua, R. Barker, and A. Neville, "Comparison of corrosion behaviour for X-65 carbon steel in supercritical CO_2-saturated water and water-saturated/unsaturated supercritical CO_2", The Journal Of Supercritical Fluids, 97, (2015): p. 224-237.
3. Y. Hua, R. Barker, and A. Neville, "Relating iron carbonate morphology to corrosion characteristics for water-saturated supercritical CO_2 systems", The Journal Of Supercritical Fluids, 98, (2015).
4. Y. Hua, R. Barker, and A. Neville, "The influence of SO_2 on the tolerbale water content to avoid pipeline corrosion during the transportation of supercritical CO_2", International Journal of Greenhouse Gas Control, 37, (2015): p. 412-423.
5. Y. Hua, R. Barker, and A. Neville, "The effect of O_2 content on the corrosion behaviour of X65 and 5Cr in water-containing supercritical CO_2 environments", Applied Surface Science, 356, (2015): p. 499-511.

6. Y. Hua, R. Barker, and A. Neville, "Effect of temperature on the critical water content for general and localised corrosion of X65 carbon steel in the transport of supercritical CO_2", International Journal of Greenhouse Gas Control, 31, (2014): p. 48-60.
7. Y. Hua, R. Barker, and A. Neville, "Understanding the influence of SO_2 and O_2 on the corrosion of carbon steel in water-saturated supercritical CO_2", Corrosion, 71, 5 (2014): p. 667-683.
8. M. Halseid, A. Dugstad, and B. Morland, "Corrosion and bulk phase reactions in CO_2 transport pipelines with impurities: Review of recent published studies", Energy Procedia, 63, (2014): p. 2557-2569.
9. J. Brown, B. Graver, E. Gulbrandsen, A. Dugstad, and B. Morland, "Update of DNV Recommended Practice RP-J202 with focus on CO_2 corrosion with impurities", Energy Procedia, 63, (2014): p. 2432-2441.
10. A. Dugstad, M. Halseid, and B. Morland, "Effect of SO_2 and NO_2 on corrosion and solid formation in dense phase CO_2 pipelines", Energy Procedia, 37, (2013): p. 2877-2887.
11. A. Dugstad, M. Halseid, B. Morland, and A.O. Sivertsen, "Corrosion in dense phase CO_2 – the impact of depressurisation and accumulation of impurities", Energy Procedia, 37, 0 (2013): p. 3057-3067.
12. A. Dugstad, B. Morland, and S. Clausen, "Corrosion of transport pipelines for CO_2 - Effect of water ingress", Energy Procedia, 4, (2011): p. 3063-3070.
13. A. Dugstad, S. Clausen, and B. Morland. "Transport of dense phase CO_2 in C-steel pipelines - when is corrosion an issue?", CORROSION 2011, paper no. 70, (Houston, TX:NACE, 2011).
14. Y.-S. Choi, S. Hassani, T.N. Vu, and S. Nesic. "Effect of H_2S on the corroison behavior of pipeline steels in supercritical and liquid CO_2 environments", CORROSION 2015, paper no. 5927, (Dallas, TX: NACE, 2015).
15. S. Sim, I.S. Cole, Y.S. Choi, and N. Birbilis, "A review of the protection strategies against internal corrosion for the safe transport of supercritical CO_2 via steel pipelines for CCS purposes", International Journal of Greenhouse Gas Control, 29, (2014): p. 185-199.

16. Y.-S. Choi, S. Nešić, and D. Young, "Effect of impurities on the corrosion behavior of CO_2 transmission pipeline steel in supercritical CO_2–water environments", Environmental Science & Technology, 44, 23 (2010): p. 9233-9238.
17. Y. Xiang, Z. Wang, Z. Li, and W. Ni, "Effect of temperature on corrosion behaviour of X70 steel in high pressure CO2/SO2/O2/H2O environments", Corrosion Engineering, Science and Technology, 48, 2 (2013): p. 121-129.
18. Y. Xiang, Z. Wang, X. Yang, Z. Li, and W. Ni, "The upper limit of moisture content for supercritical CO_2 pipeline transport", The Journal of Supercritical Fluids, 67, (2012): p. 14-21.
19. Y. Xiang, Z. Wang, Z. Li, and W.D. Ni, "Effect of Exposure Time on the Corrosion Rates of X70 Steel in Supercritical CO_2/SO_2/O_2/H_2O Environments", Corrosion, 69, 3 (2012): p. 251-258.
20. Y. Xiang, Z. Wang, C. Xu, C. Zhou, Z. Li, and W. Ni, "Impact of SO_2 concentration on the corrosion rate of X70 steel and iron in water-saturated supercritical CO_2 mixed with SO_2", The Journal of Supercritical Fluids, 58, 2 (2011): p. 286-294.
21. F.W. Schremp and G.R. Roberson, "Effect of supercritical carbon dioxide (CO_2) on construction materials", SPE, 15, 3 (1975): p. 227-233.
22. A. Oosterkamp and J. Ramsen, "State-of-the-art overview of CO_2 pipeline transport with relevance to offshore pipelines", Polytech Report No: POL-O-2007-138-A, (2008).
23. E. de Visser, C. Hendriks, M. Barrio, M.J. Mølnvik, G. de Koeijer, S. Liljemark, and Y. Le Gallo, "Dynamis CO_2 quality recommendations", International Journal of Greenhouse Gas Control, 2, 4 (2008): p. 478-484.
24. Kinder Morgan, "CO_2 Transportation pipelines", [Online], Available at: http://www.kindermorgan.com/business/co2/transport.cfm. Accessed on 11th March 2015.
25. S. Walspurger and H.A.J.v. Dijk, "EDGAR CO_2 purity: type and quantities of impurities related to CO_2 point source and capture technology: a literature study", ECN-E-12-054, (2012).

26. N. Spycher, K. Pruess, and J. Ennis-King, "CO_2-H_2O mixtures in the geological sequestration of CO_2. I. Assessment and calculation of mutual solubilities from 12 to 100°C and up to 600 bar", Geochimica et Cosmochimica Acta, 67, 16 (2003): p. 3015-3031.
27. ASTM, Standard G1-03, Standard practice for preparing, cleaning, and evaluating corrosion test specimens. ASTM International: West Conshohocken, PA, 2003.
28. G. Schmitt and R. Forster. "Unexpected Effect of Small Oxygen Concentrations in Sales Gas on Element Currents between Pipeline Steel and Magnetite from Black Powder", CORROSION 2015: NACE International, 2015).
29. C.H. Chio, S.K. Sharma, and D.W. Muenow, "The hydrates and deuterates of ferrous sulfate (FeSO4): a Raman spectroscopic study", Journal of Raman Spectroscopy, 38, 1 (2007): p. 87-99.
30. ASTM, Standard G46-94, Standard guide for examination and evaluation of pitting corrosion. ASTM International: West Conshohocken, PA, 2003.
31. OLI is a commercial software package from Corr Science, for more information see: http://www.corrscience.com/products/oli/.
32. R. Barker, Y. Hua, and A. Neville, Internal corrosion of carbon steel pipelines for dense-phase CO_2 transport in carbon capture and storage (CCS)–a review. International Materials Reviews, 2017. **62**(1): p. 1-31.
33. Xu, M., Q. Zhang, X. Yang, Z. Wang, J. Liu, and Z. Li, *Impact of surface roughness and humidity on X70 steel corrosion in supercritical CO 2 mixture with SO 2, H 2 O, and O 2.* The Journal of Supercritical Fluids, 2016. **107**: p. 286-297.
34. Sun, C., J. Sun, Y. Wang, X. Lin, X. Li, X. Cheng, and H. Liu, Synergistic effect of O2, H2S and SO2 impurities on the corrosion behavior of X65 steel in water-saturated supercritical CO2 system. Corrosion Science, 2016.

35. Sun, J., C. Sun, G. Zhang, X. Li, W. Zhao, T. Jiang, H. Liu, X. Cheng, and Y. Wang, Effect of O2 and H2S impurities on the corrosion behavior of X65 steel in water-saturated supercritical CO2 system. Corrosion Science, 2016. **107**: p. 31-40.

36. Sun, C., Y. Wang, J. Sun, X. Lin, X. Li, H. Liu, and X. Cheng, Effect of impurity on the corrosion behavior of X65 steel in water-sa*turated supercritical CO2 system.* The Journal of Supercritical Fluids, 2016. **116**: p. 70-82.

37. Farelas. F, Choi. Y.-S., and Nešić. S, Corrosion Behavior of API 5L X65 Carbon Steel under Supercritical and Liquid Carbon Dioxide Phases in the Presence of Water and Sulfur Dioxide. Corrosion, 2012. **69**(3): p. 243-250.

38. Farelas. F, Choi Y.-S., and Nesic. S, "Effects of CO_2 phase change, SO_2 content and flow on the corrosion of CO_2 transmission pipeline steel", in CORROSION 2012. 2012: Salt Lake City, UT:NACE.

422 **Table 1: Elemental composition (wt.%) of API 5L X65 carbon steel and UNS41000 13Cr**

	X65	13Cr
C	0.12	0.15
Si	0.18	0.36
Mn	1.27	0.56
P	0.008	0.006
S	0.002	0.008
Cr	0.11	13.5
Mo	0.17	-
Fe	Balance	

423

424 **Table 2: Test matrix for corrosion experiments in water-saturated dense phase CO_2**

Temperature (°C)	Pressure (bar)	Materials	H_2O (ppm)	SO_2 (ppm)	O_2 (ppm)	Immersion time hours
35	80	X65/13Cr	Above solubility limit of 3437ppm through addition of 34000ppm water	0	0	48
				0	1000	
				100	0	
				100	1000	
Temperature (°C)	**Pressure (bar)**	**Materials**	**H_2O (ppm)**	**SO_2 (ppm)**	**O_2 (ppm)**	**Immersion time hours**
35	80	X65/13Cr	Above solubility limit of 3437ppm through addition of 34000ppm water	100	1000	6/14/24/48

425

426

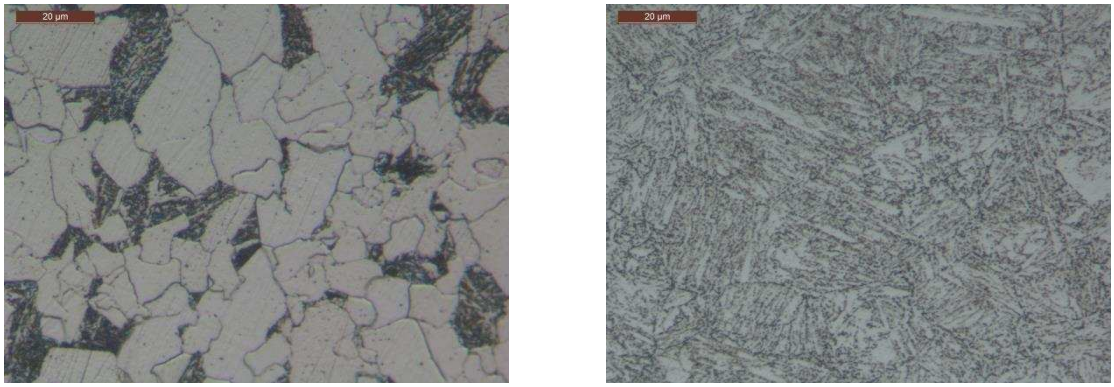

(a) (b)

427 **Figure 1: Microstructure of a) API 5L X65 – depicting a ferritic-pearlitic structure and b) UNS41000**

428 **13Cr – depicting a martensitic structure**

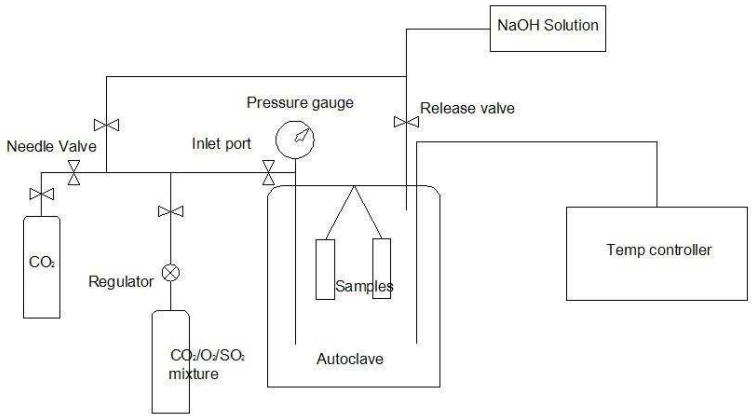

429

430 **Figure 2: Schematic of the autoclave setup for impure, dense phase CO_2 experiments**

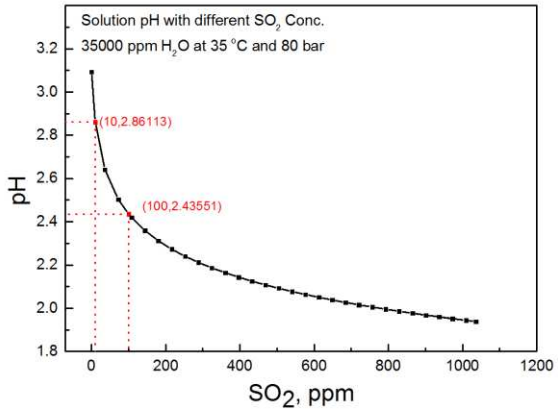

431

432 **Figure 3: Predicted pH of CO_2-saturated water in the presence of SO_2 at 35°C and 80 bar**

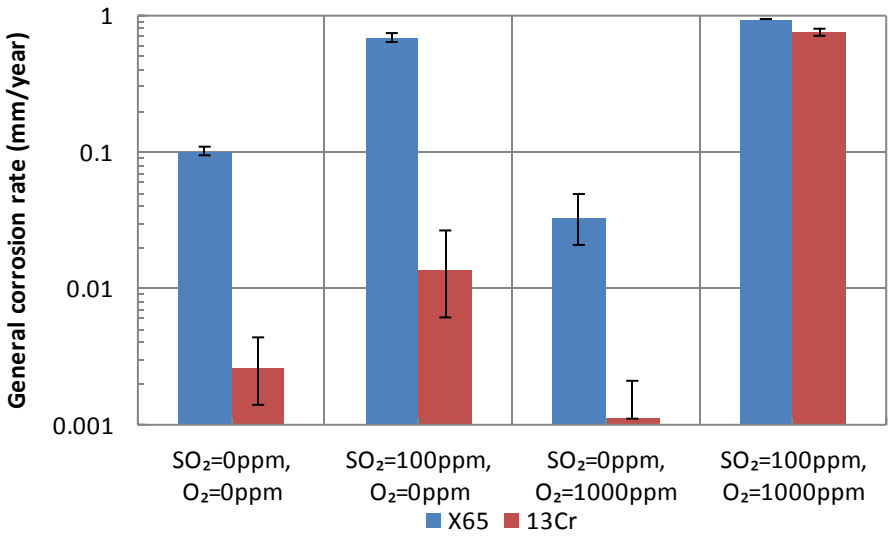

Figure 4: General corrosion rates of X65 and 13Cr after exposure to water-saturated dense phase CO_2 at 80 bar and 35 °C for 48 h in the presence of various concentrations of SO_2 and O_2

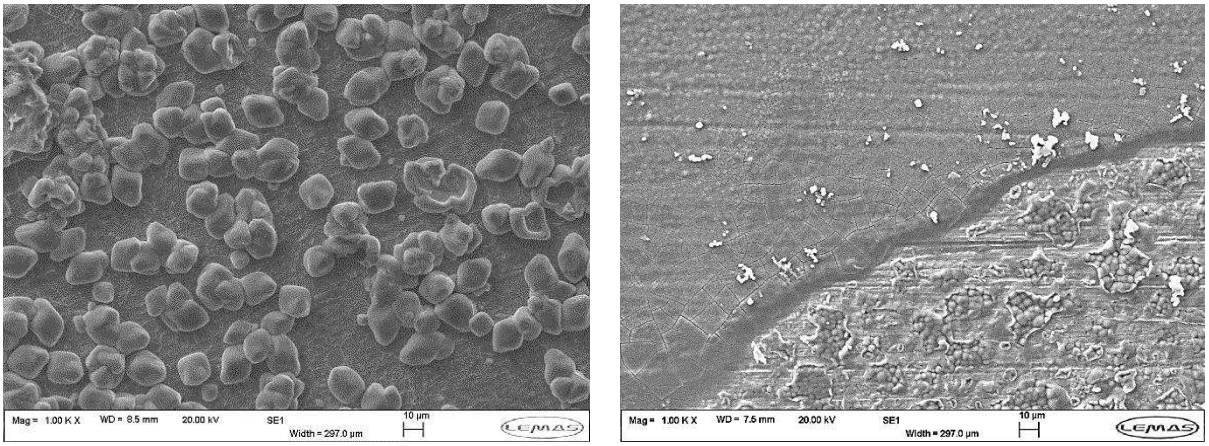

(a) **(b)**

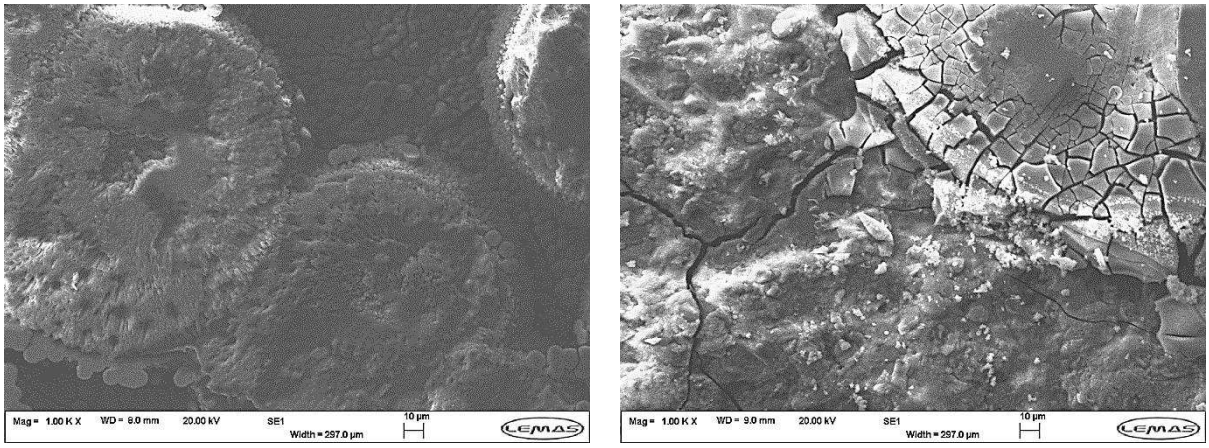

(c) **(d)**

Figure 5: SEM images of X65 samples exposed to water-saturated supercritical CO_2 conditions at 80 bar and 35°C containing (a) 0 ppm SO_2 and 0 ppm O_2; (b) 0 ppm SO_2 and 1000 ppm O_2; (c) 100 ppm SO_2 and 0 ppm O_2 and (d) 100 ppm SO_2 and 1000 ppm O_2

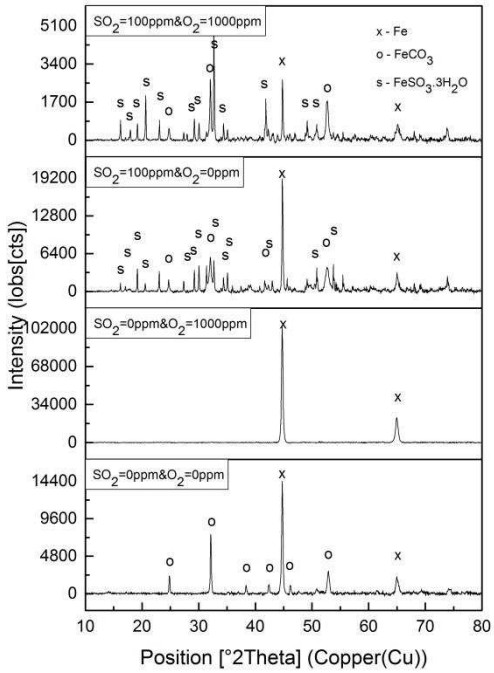

Figure 6: XRD patterns of X65 samples exposed to water-saturated supercritical CO_2 containing various SO_2 and O_2 at 35°C and 80 bar after 48 h

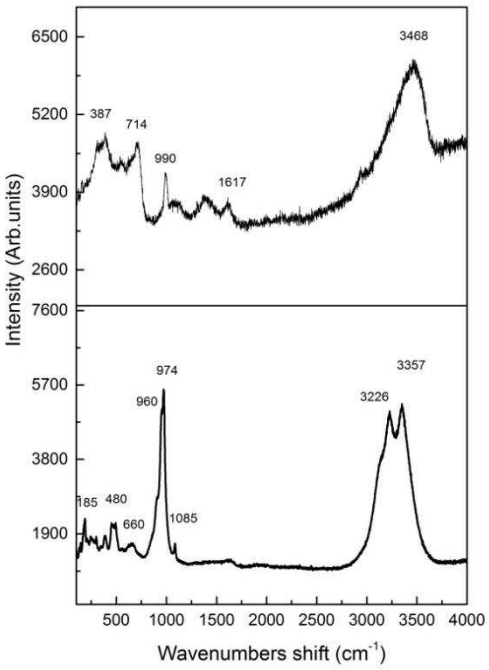

449

450 **Figure 7: Raman spectra of X65 sample exposed to water-saturated supercritical CO_2**
451 **containing 100 ppm SO_2 and 1000 ppm O_2 at 35°C and 80 bar after 48 h**
452

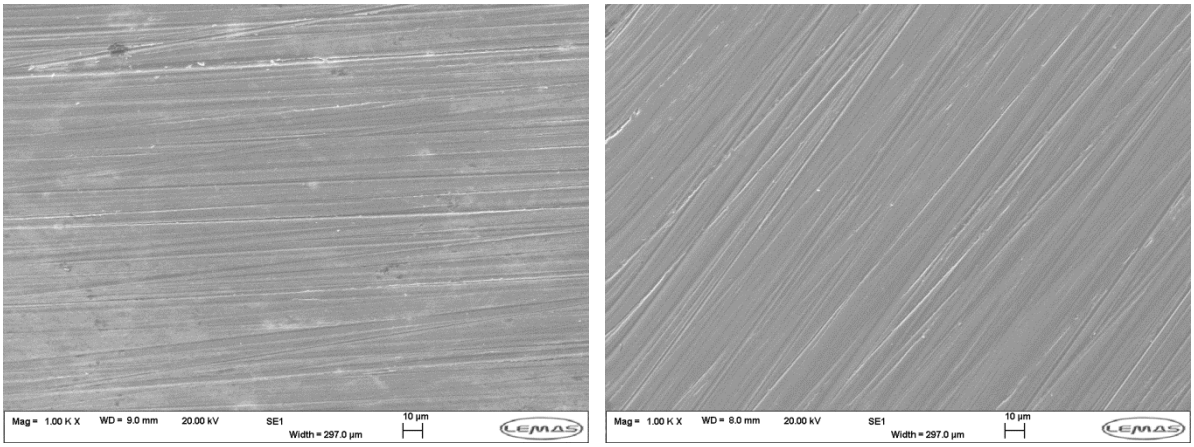

(a) **(b)**

453 **Figure 8: SEM images of 13Cr samples exposed to water-saturated supercritical CO_2**
454 **condition with, (a) 0 ppm SO_2 and 0 ppm O_2 and (b) 0 ppm SO_2 and 1000 ppm O_2 after 48 h**
455
456

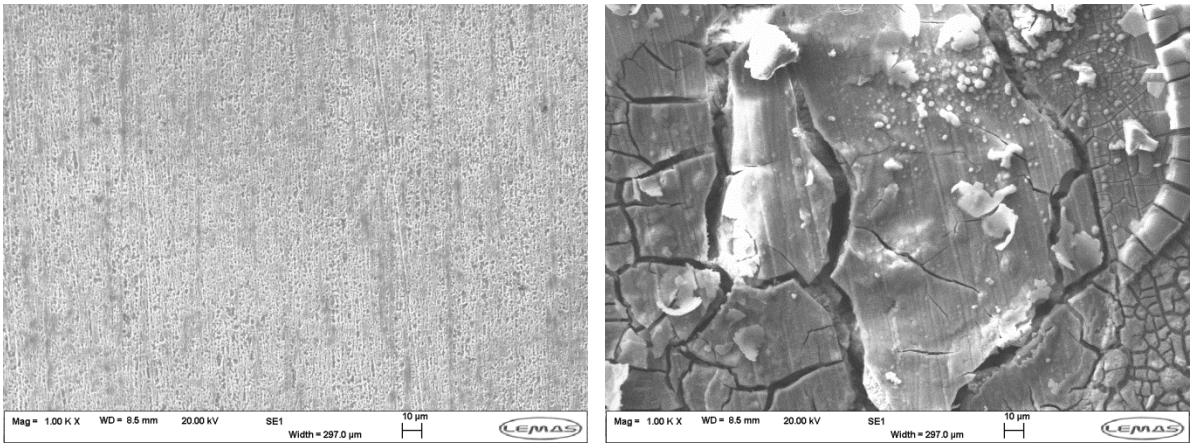

(a) **(b)**

457 **Figure 9: SEM images of 13Cr samples exposed to water-saturated supercritical CO_2**
458 **condition with (a) 13Cr - 100 ppm SO_2 and 0 ppm O_2, (b) 13Cr - 100 ppm SO_2 and 1000 ppm**
459 **O_2 after 48 h**

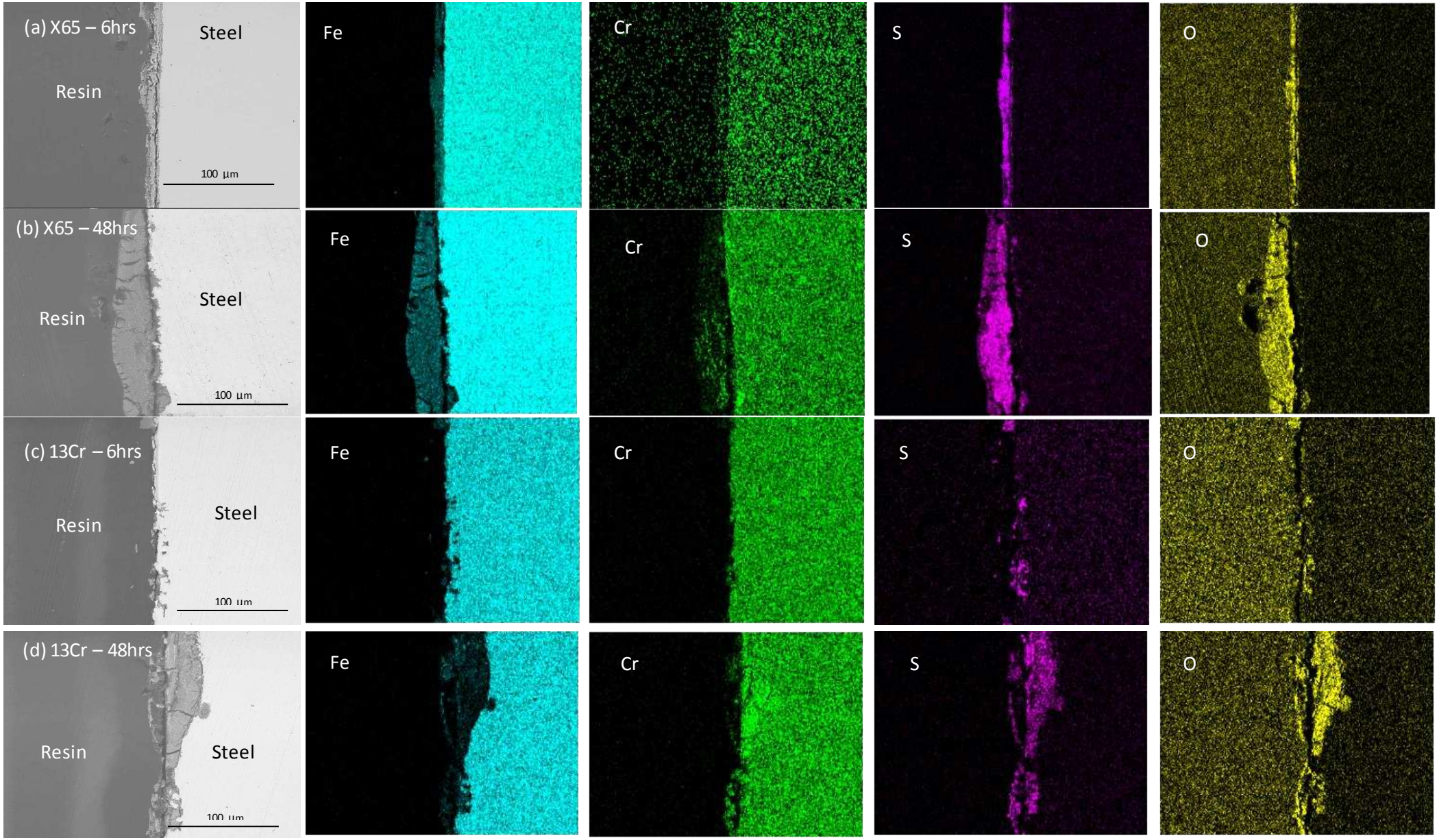

Figure 10: SEM cross-section images of (a) X65 – 6 hours, (b) X65 – 48 hours, (c) 13Cr – 6 hours and (d) 13Cr – 48 hours samples exposed to water-saturated supercritical CO_2 at 80 bar and 35°C with 100 ppm SO_2 and 1000 ppm O_2.

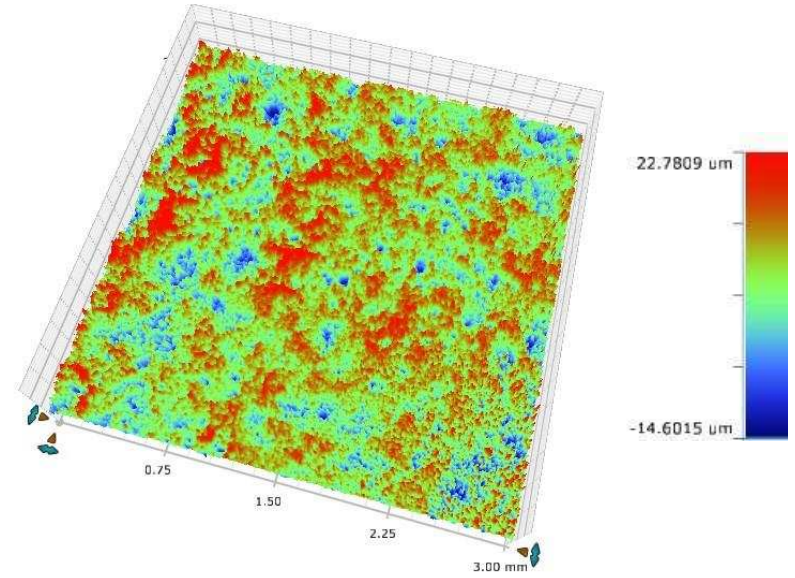

(a)

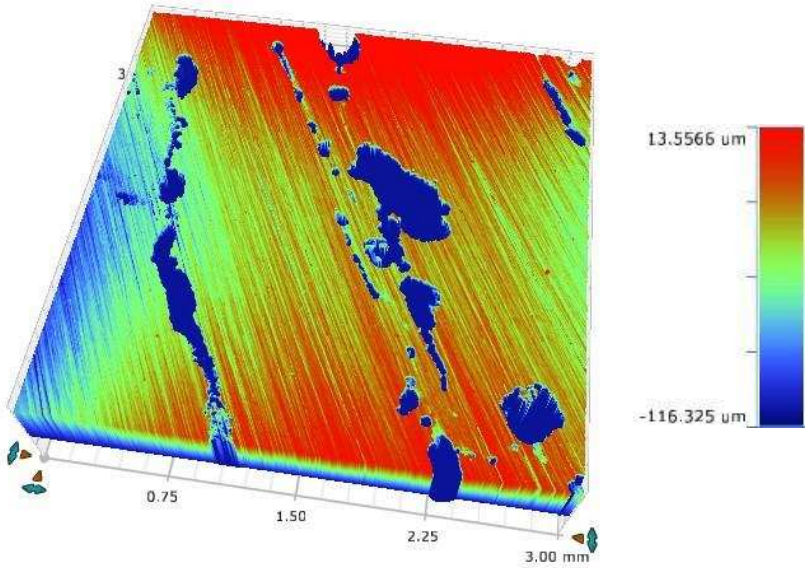

(b)

Figure 11: Examples of profilometry images (after removal of corrosion products) from (a) X65 and (b) 13Cr after exposure to water-saturated supercritical CO_2 in the presence of 100 ppm SO_2 and 1000 ppm O_2 at 35°C and 80 bar for 48 h

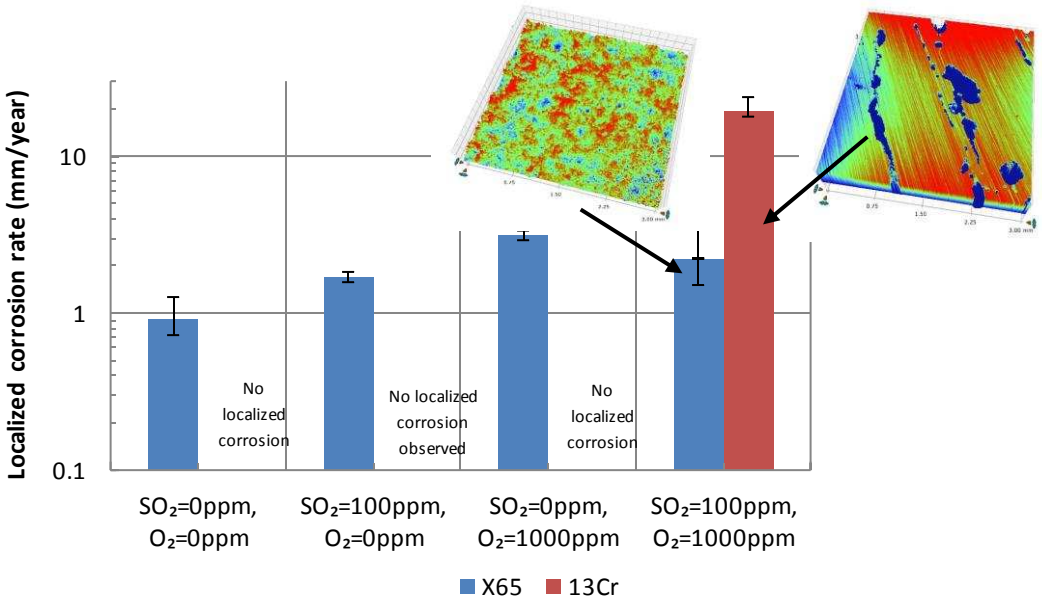

Figure 12: Localized corrosion rates of X65 and 13Cr in water-saturated supercritical CO_2 environments containing varying concentrations of SO_2 and O_2 at 35°C and 80 bar for 48 h

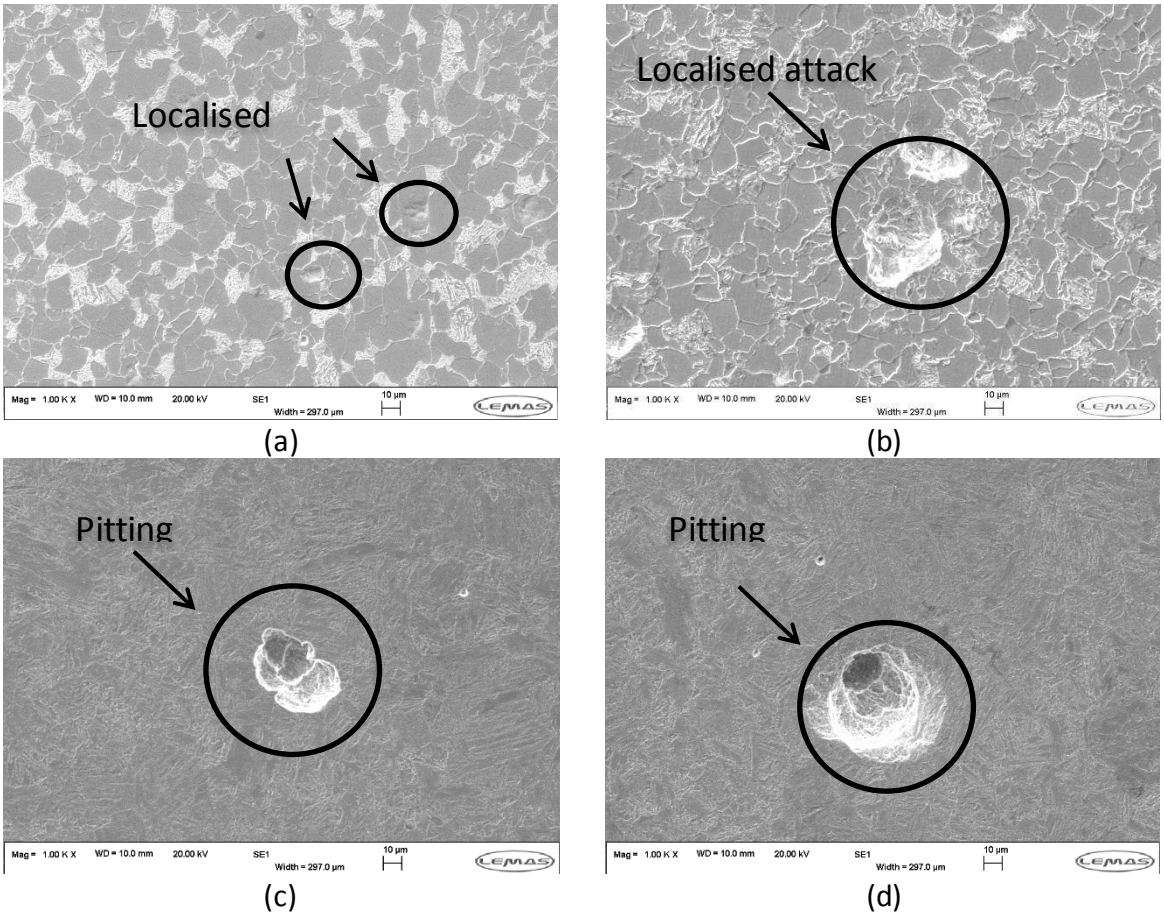

Figure 13: SEM images of samples (after removal of the corrosion products) exposed to water-saturated supercritical CO_2 condition with 100 ppm SO_2 and 1000 ppm O_2 (a) X65 – 6 h, (b) X65 - 48 h, (c) 13Cr – 6 h and (d) 13Cr – 48 h

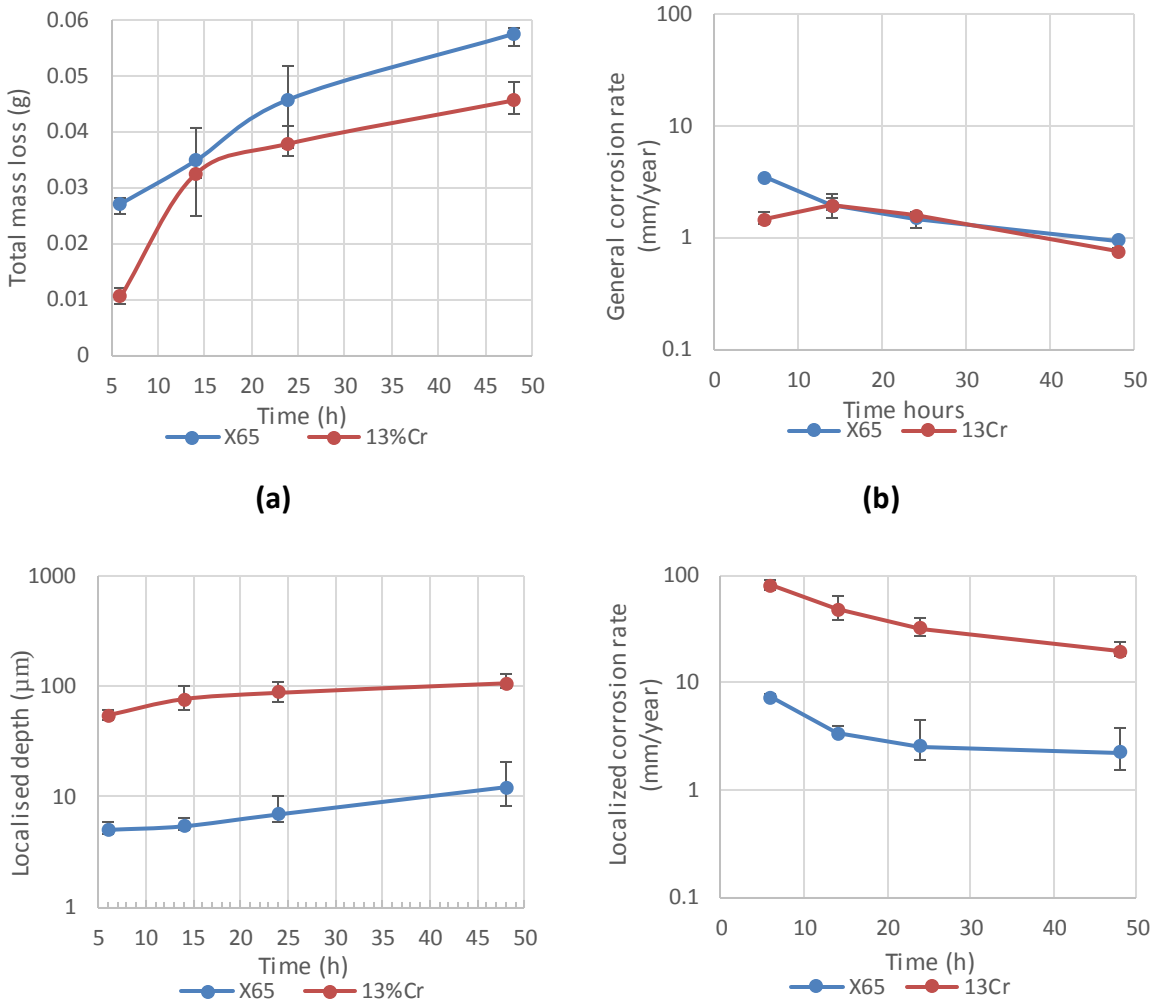

Figure 14: (a and b) Total mass loss and general corrosion rates and (c and d) localized depth and localized corrosion rates of X65 and 13Cr in water-saturated supercritical CO_2 in the presence of 100 ppm SO_2 and 1000 ppm O_2 at 80 bar and 35 °C for exposure times of 6, 14, 24 and 48 h

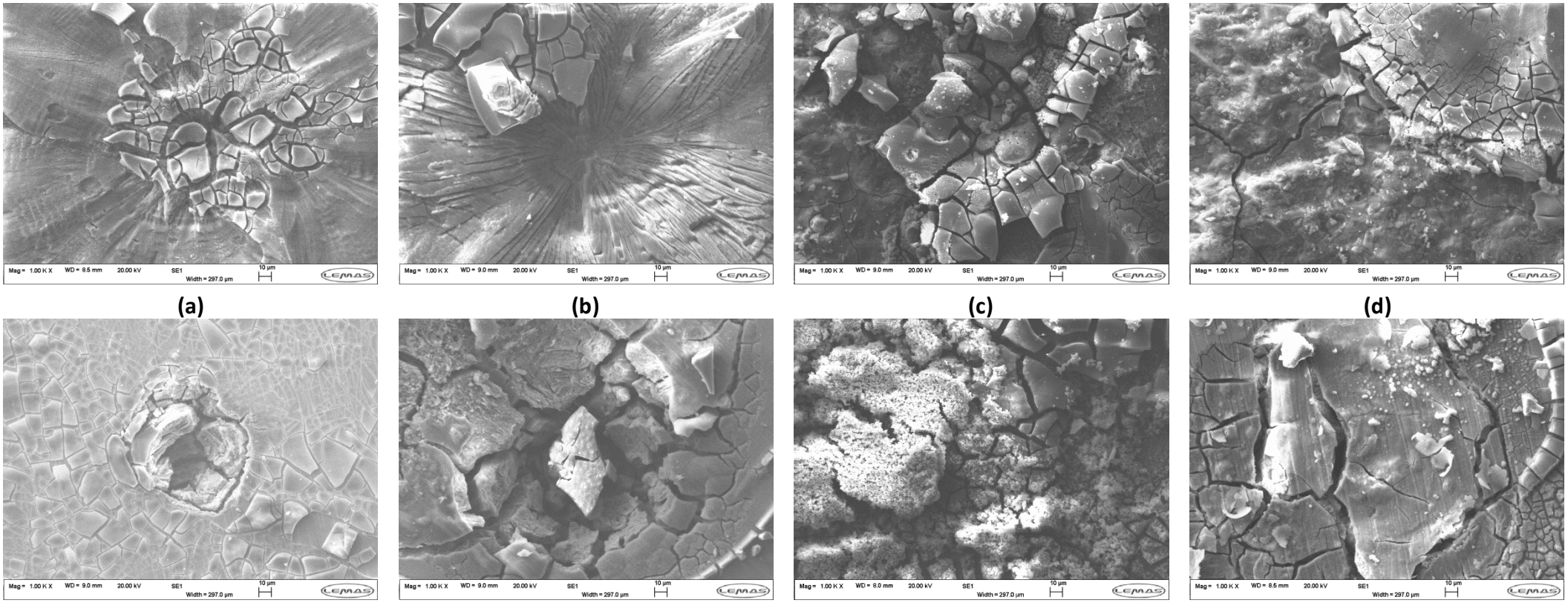

Figure 15: SEM images of samples exposed to water-saturated supercritical CO_2 with 100 ppm SO_2 and 1000 ppm O_2 (a) X65 – 6 h, (b) X65 – 14 h, (c) X65 – 24 h, (d) X65 – 48 h, (e) 13Cr – 6 h, (f) 13Cr – 14 h, (g) 13Cr – 24 h, and (h) 13Cr – 48 h

1